Semiclassical description of angle-dependent magnetoresistance oscillations in quasi-one-dimensional metals

S. J. Blundell and J. Singleton
Clarendon Laboratory, Parks Road, Oxford OX1 3PU, United Kindgom
(Received 14 August 1995)

We use a semiclassical model to calculate the angle-dependent magnetoresistance oscillations (AMROs) in quasi-one-dimensional (q1D) organic conductors. A number of contrasting models have been proposed to explain this effect, mainly in the context of the $(TMTSF)_2X$ (where TMTSF is tetramethyltetraselenafulvalene and $X=ClO_4$ or PF_6) family; some of the models concentrate on the role of electron-electron interactions while others postulate Fermi-surface hotspots or even field-dependent hopping renormalization. Instead, we have used a more intuitive semiclassical approach to calculate the angle-dependent magnetoresistance oscillations for a completely general class of q1D Fermi surfaces. The model demonstrates how the details of the Fermi surface corrugation give particular features in the experimental data and illustrates the important roles played by both open and closed orbits. The AMRO observed in $(TMTSF)_2ClO_4$ when the magnetic field is rotated close to the *a* axis are discussed in this context. The results are particularly applied to the organic charge transfer salt $(ET)_2KHg(SCN)_4$ [where ET is bis(ethylenedithio)tetrathiafulvalene]; this material is interesting because the Fermi surface undergoes a transition from predominantly q1D to quasi-two-dimensional (q2D) character at ~22 T, a result which has been primarily established on the basis of AMRO experiments. Higher order Fourier components in the corrugation of the Fermi sheet are shown to be essential to explain the observed AMROs and the size of the magnetoresistance in this material. The absence of q1D AMROs in most organic metals with q1D Fermi surfaces is explained, illustrating in particular why q1D AMROs are absent above 22 T in $(ET)_2KHg(SCN)_4$ even though the Fermi surface contains q1D sections. We discuss the failure of previous models to explain the AMRO effect in this salt and demonstrate the advantages of adopting a semiclassical approach.

I. INTRODUCTION

In the last 40 years, magnetoresistance (MR) experiments have been particularly useful in determining the shape of the Fermi surface (FS) of metals.[1] The presence of open and closed orbits can be easily distinguished by the field dependence of the MR while the area of the FS pockets can be measured by the frequency of Shubnikov–de Haas oscillations (SdHOs).[2] Recently, these techniques have been applied to organic metals.[3] SdHOs can be used to determine information concerning the FS geometry because the frequency of each series of oscillations is proportional to the area of an *extremal orbit* of the FS.[2] The orbits which are not extremal do not contribute to this oscillatory signal but give rise to the non-oscillatory background MR. However, this background MR can depend quite dramatically on the *direction* of the applied magnetic field, and in some cases very large angle-dependent magnetoresistance oscillations (AMROs) at constant field can be found.

Experimentally, AMROs are measured by rotating a sample in a fixed magnetic field while monitoring the resistivity of the sample. AMROs can be observed at much higher temperatures and in much lower applied fields than SdHOs.[3] SdHOs arise from the movement of well-resolved Landau levels through the Fermi energy and therefore require that the temperature is low enough for the FS to be sharply defined; this restriction does not apply so stringently to AMROs since they do not originate from the motion of energy levels through the FS. The information obtained from AMROs can therefore be complementary to SdHOs since the effect is due to all electrons on the FS, not just those performing extremal orbits.

For example, AMRO studies have provided additional shape information about the warping of cylindrical sections of the quasi two-dimensional (q2D) FS in organic conductors due to the behavior of electrons in closed orbits around these cylinders.[4,5] In a number of other ''quasi-one-dimensional'' (q1D) conductors, the FS is dominated by q1D sheets across which electrons may also perform open orbits. In these materials, a different type of AMROs is observed which must have an origin quite distinct from that responsible for AMROs in metals with a q2D FS.

First studied in this context were the q1D AMRO in the organic conductors $(TMTSF)_2X$ (where TMTSF is tetramethyltetraselenafulvalene and $X=ClO_4$ or PF_6). These materials are of enormous interest because they can exhibit superconductivity, a cascade of field-induced spin density waves, and even the quantum Hall effect, under different conditions of pressure, field, and temperature.[6–8] The TMTSF salts are highly anisotropic and consist of stacks of TMTSF molecules along the highly conducting direction (along *a*); the stacks are assembled into sheets which are themselves separated by the anion *X* layers along the least conducting direction (i.e., along *c*). The bandwidths are typically in the ratio $t_a:t_b:t_c=1:0.1:0.003$ eV. Sharp AMROs have been observed, consisting of resistance dips at particular ''magic angles'' of the applied magnetic field to the crystal axes of these materials.[9–11] When the magnetic field direction is at a magic angle, the electron motion in the q1D

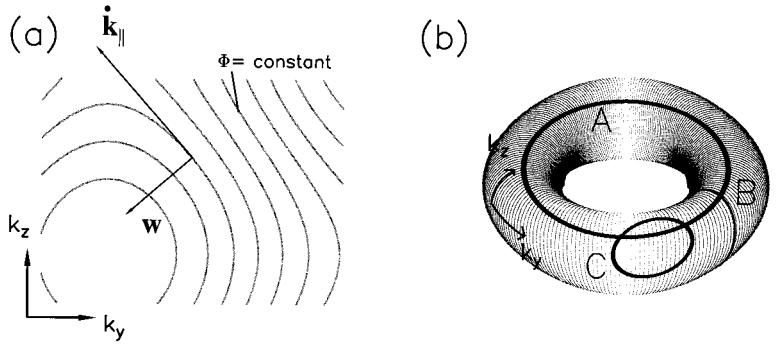

FIG. 1. (a) Schematic showing electron trajectories in the k_y-k_z plane. The vectors $\dot{\mathbf{k}}_\parallel=(e/\hbar)\mathbf{w}\times\hat{\mathbf{i}}$ and $\mathbf{w}=v_F\mathbf{B}_\parallel+B_\perp\nabla_{\mathbf{k}_\parallel}f$ are also shown. The electron motion is along contour lines of constant Φ. (b) Types of FS orbits on the Brillouin zone (represented by a torus). Orbit *C* is contractible and corresponds to a closed orbit. Orbits *A* and *B* correspond to open orbits.

planes becomes periodic in the reduced zone scheme; away from these magic angles, the electron orbits sweep out the entire Brillouin zone ergodically. It is this principle which is at the basis of most explanations of the effect, but theoretical treatments sometimes additionally stress the role of electron-electron interactions, FS hotspots, or non-Fermi liquid behavior. [12–20]

Q1D AMROs have also been studied[21,22,25,26] in the low temperature phase of $(ET)_2KHg(SCN)_4$, which is a charge transfer salt of the organic molecule ET (where ET is bis-(ethylenedithio)tetrathiafulvalene, known also as BEDT-TTF). This salt consists of alternating sheets[24] of ET molecules and the anion $KHg(SCN)_4$. For reasons which we discuss later, the AMROs in this particular material may be easier to understand than those in TMTSF salts.

In this paper, we describe a purely semiclassical approach to AMROs in q1D metals. The orbits of all electrons on the FS are calculated by considering the Lorentz force $-e\mathbf{v}(\mathbf{k})\times\mathbf{B}$, and the conductivity is then calculated by using the Boltzmann transport equation. Thus electron-electron interactions are entirely neglected and a $\mathbf{k}$-independent scattering time is assumed (i.e., no FS hotspots). Thus the conductivity is straightforward to calculate and a comparison with experimental data can be made. This is useful not least because a proper examination of the consequences of a semiclassical model *may* lead to a recognition of its failure to describe certain real systems; this could then provide a legitimate motivation for the use of more exotic mechanisms.

The use of a semiclassical method to understand AMROs in TMTSF salts was pioneered by Osada *et al.*[18] Recently, similar techniques were ingeniously used to explain newly discovered resonances in $(TMTSF)_2ClO_4$ when the magnetic field direction was rotated close to the *a* axis.[23] Here we aim to relate the geometric structure of the FS, as parametrized by the Fourier components of the FS corrugation, directly to features in the angle-dependent conductivity. We also attempt to classify the types of FS orbits induced by the magnetic field and apply our results to $(ET)_2KHg(SCN)_4$.

This paper is organized as follows: some general considerations and the method of calculation are presented in Sec. II; this method is applied first to a simplified model consisting of a FS with a weak corrugation in Sec. III, the general case being considered in Sec. IV; the results are discussed in Sec. V in the context of recent experiments.

II. THEORY

Consider the linearized q1D FS described by the following energy dispersion relation:

$$E(\mathbf{k})/\hbar=v_F(|k_x|-k_F)-f(k_y,k_z). \tag{1}$$

The FS [defined by $E(\mathbf{k})=0$] consists of two flat sheets at $k_x=\pm k_F$ which are slightly warped in a manner described by the function f (we assume throughout that $|f(k_y,k_z)|\ll k_Fv_F$ so that the two sheets do not touch). The velocity $\mathbf{v}(\mathbf{k})$ of each electron as a function of momentum $\mathbf{k}$ can then be calculated using

$$\mathbf{v}(\mathbf{k})=\hbar^{-1}[dE(\mathbf{k})/d\mathbf{k}]=\pm v_F\hat{\mathbf{i}}-\nabla_{\mathbf{k}_\parallel}f, \tag{2}$$

where $\nabla_{\mathbf{k}_\parallel}\equiv(0,\partial/\partial k_y,\partial/\partial k_z)$ and $\hat{\mathbf{i}}$ is a unit vector in the k_x direction. (In what follows, we will consider only one sheet for which $k_x\sim+k_F$ without loss of generality.) The velocity will be time dependent since the electron's momentum $\mathbf{k}$ varies with time according to the equation of motion

$$\hbar\dot{\mathbf{k}}=-e\mathbf{v}\times\mathbf{B} \tag{3}$$

with the magnetic field $\mathbf{B}$ given by

$$\mathbf{B}=B_\perp\hat{\mathbf{i}}+\mathbf{B}_\parallel. \tag{4}$$

This equation of motion implies that $\dot{\mathbf{k}}$ remains perpendicular to $\mathbf{v}$; this condition ensures that the electron remains on the FS. For this reason, we need only calculate the equation of motion for $\mathbf{k}_\parallel=(0,k_y,k_z)$ since the k_x component can always be calculated using $k_x=k_F+f(k_y,k_z)/v_F$. Therefore we find that the equation of motion [Eq. (3)] can be written as

$$\dot{\mathbf{k}}_\parallel=\frac{e}{\hbar}\mathbf{w}\times\hat{\mathbf{i}}, \tag{5}$$

where the vector field $\mathbf{w}$ also lies in the plane of the sheet and is given by

$$\mathbf{w}=v_F\mathbf{B}_\parallel+B_\perp\nabla_{\mathbf{k}_\parallel}f. \tag{6}$$

The vector field $\dot{\mathbf{k}}_\parallel$ is solenoidal ($\nabla\cdot\dot{\mathbf{k}}_\parallel=\nabla_{\mathbf{k}_\parallel}\cdot\dot{\mathbf{k}}_\parallel=0$) so that $\dot{\mathbf{k}}_\parallel$ is an area-preserving flow;[27] the vector field $\mathbf{w}$ is conservative ($\nabla\times\mathbf{w}=\nabla_{\mathbf{k}_\parallel}\times\mathbf{w}=0$) so that we can define a scalar function Φ such that $\mathbf{w}=\nabla\Phi$ where

$$\Phi=v_F\mathbf{B}_\parallel\cdot\mathbf{k}_\parallel+B_\perp f \tag{7}$$

so that the electron motion is along contour lines of constant Φ [see Fig. 1(a)]. In the simple case where the magnetic field lies in the plane of the sheets ($B_\perp=0$), the vector field $\mathbf{w}=v_F\mathbf{B}_\parallel$ is constant so that electrons appear to travel in straight lines across the Fermi sheet in a direction perpendicular to $\mathbf{B}=\mathbf{B}_\parallel$ when viewed along k_x.

Because of the periodicity of the Brillouin zone, we can identify the state (k_y,k_z) with states at $(k_y+m\pi/b,k_z+n\pi/c)$ (where m and n are integers) and so the electron dynamics across the Fermi sheet can be understood by considering the vector fields $\dot{\mathbf{k}}$ and $\mathbf{w}$ defined on a torus T^2 (the scalar function Φ is, however, multiple-valued on T^2). Using the fact that the Euler-Poincaré characteristic of a torus $\chi(T^2)$ is zero, then if the vector fields have only isolated singular points, then it may be shown that the number of maxima plus the number of minima minus the number of saddle points in Φ is equal to $\chi(T^2)=0$.

Different types of FS orbits are possible. Orbits can be represented as loops on the torus and can be topologically characterized by two *winding numbers* [28] (we will denote these η_y and η_z; they describe the number of times the loop winds around the torus in the k_y and k_z directions, respectively). Three such orbits are shown in Fig. 1(b): the loop C is contractible to a point (it has $\eta_y=\eta_z=0$) and corresponds to a closed orbit; in contrast, the loops A and B are not contractible (they both have one unit winding number: for A $\eta_y=1$, $\eta_z=0$, for B $\eta_y=0$, $\eta_z=1$) and correspond to open orbits. Further open orbits are also possible which can wind round the torus many times in either (or both) directions.

Having characterized the shape of the FS orbits for a particular orientation of the magnetic field, the conductivity can be calculated using the Boltzmann transport equation:

$$\sigma_{ij}=\frac{e^2}{4\pi^3}\int_{\mathrm{FS}} d\mathbf{k}^3\left[-\frac{\partial f_0(\mathbf{k})}{\partial E(\mathbf{k})}\right]v_i(\mathbf{k},0)\int_{-\infty}^{0} v_j(\mathbf{k},t)e^{t/\tau}dt. \tag{8}$$

This is an integral (over all states at the FS) of the velocity-velocity correlation function for each FS orbit. This can change dramatically as the direction of the magnetic field is changed, because this alters the paths of all the FS orbits.

We can also express a general q1D FS by expressing the function $f(k_y,k_z)$ in Fourier components:

$$E(\mathbf{k})=\hbar v_F(|k_x|-k_F)-\sum_{m,n}\left[t_{mn}^{\mathrm{even}}\cos(mbk_y+nck_z)\right.$$
$$\left.+t_{mn}^{\mathrm{odd}}\sin(mbk_y+nck_z)\right], \tag{9}$$

where the parameters t_{mn}^{even} and t_{mn}^{odd} are the even and odd Fourier components of the corrugation of the Fermi sheets. As will be described later, in certain situations the ''geometric structure'' of the orbits can have little bearing on the magnetoresistance. When the magnetic field is in the plane of the q1D sheets, then in some ''resonant'' field directions the orbits may be periodic on the reduced Brillouin zone, while at a ''general'' direction they will instead ergodically fill the whole Brillouin zone. The contribution of such a resonant orbit is governed by a particular t_{mn} and will produce no conductivity resonance if $t_{mn}=0$. We stress that it is the *geometry* of the Fermi sheet, parametrized by the Fourier components t_{mn} of the corrugation which entirely controls the AMROs with this field direction. However, with other field directions, the geometric structure of the orbit can play a major role.

Before considering the general FS of Eq. (9), in the following section we study in detail a special case.

III. WEAKLY MODULATED FERMI SHEETS

A special case of Eq. (9) can be obtained if the only nonzero Fourier components of the corrugation are $t_{10}^{\mathrm{even}}=2t_b$ and $t_{01}^{\mathrm{even}}=2t_c$. This model has been extensively used to study the $(\mathrm{TMTSF})_2X$ family of organic conductors in which the two sheets are only weakly modulated by a single Fourier component in each of the y and z directions. The amplitude of the modulation is determined by the tight binding transfer integrals t_b and t_c, where in TMTSF salts their ratio is typically given by $t_b/t_c\sim 30$. Using our notation, we will therefore now consider the energy dispersion relation in Eq. (1) with the function f given by

$$\hbar f(k_y,k_z)=2t_b\cos(bk_y)+2t_c\cos(ck_z) \tag{10}$$

with $t_b/t_c>1$. The shape of this FS is sketched in Fig. 2(a) [a more general and more highly corrugated FS is shown in Fig. 2(b) for comparison]. The parameters t_b and t_c are transfer integrals along the b and c axes.[7]

A. Classification of orbits

With the magnetic field perpendicular to the sheets $(\mathbf{B}_\parallel=0)$ a combination of open orbits and closed orbits is allowed. The fraction of closed orbits can be easily calculated as

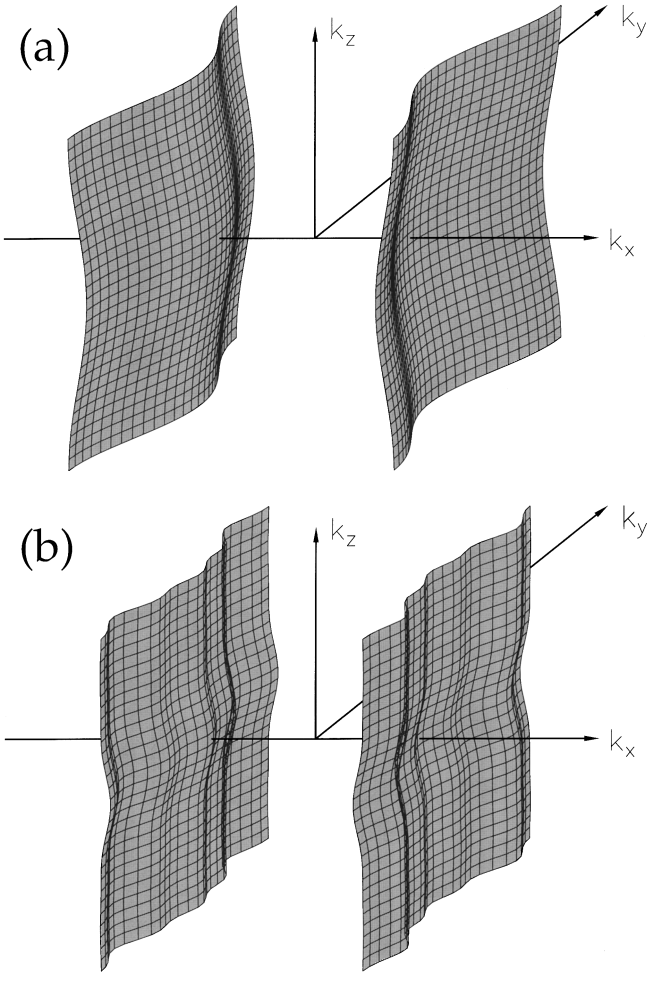

FIG. 2. (a) The FS of Eq. (10). (b) A more general FS.

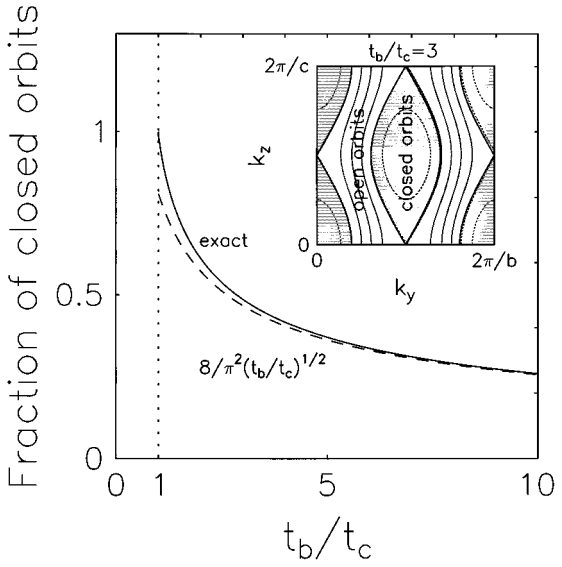

FIG. 3. The fraction of closed orbits as a function of t_b/t_c. Also shown is an approximation to the exact result which is valid for large t_b/t_c. Inset: the orbits for $t_b/t_c=3$ (which are contours of constant Φ). The region of closed orbits are shaded.

$$\frac{2c}{\pi^2}\int_0^{\pi/c} dk_z \cos^{-1}\left(1-\frac{t_c}{t_b}(1+\cos k_z c)\right) \sim \frac{8}{\pi^2(t_b/t_c)^{1/2}} \quad \text{for} \quad t_b \gg t_c \tag{11}$$

(see Fig. 3) so that the fraction of closed orbits decreases as t_b/t_c increases. This fraction is independent of the strength of the applied magnetic field $|\mathbf{B}|$. The inset to Fig. 3 shows the orbits for $t_b/t_c=3$ (the orbits are contours of constant Φ); the closed orbits have zero winding number, the open orbits have unit winding number.

As the magnetic field is rotated into the plane, the fraction of closed orbits decreases. When the parallel component of the magnetic field is sufficiently large in comparison with the perpendicular component, all the orbits are open. We will consider the case when $\mathbf{B}_\parallel=(0,0,B_\parallel)$. All the orbits then become open when

$$\frac{B_\parallel}{B_\perp} \geqslant \frac{2ct_c}{\hbar v_F} \tag{12}$$

(when $t_b/t_c>1$). This behavior is shown in Fig. 4: the inset shows the orbits for a particular choice of t_b/t_c and $B_\parallel/B_\perp$.

As the fraction of the open orbits increases, the character of these orbits changes in a very marked way. When the magnetic field is out of the plane, they lie along the k_z direction (see the inset to Fig. 3) so that their winding numbers are $\eta_y=0$ and $\eta_z=1$. However, as soon as the field acquires a nonzero component along the z direction, a transition immediately occurs and $\eta_y=1$, $\eta_z=0$. However, although the orbits are therefore now extended along the k_y direction, they still exhibit a large degree of movement in the k_z direction as illustrated in Fig. 5(a). The open orbits must navigate around isolated islands of closed orbits and each open orbit has an amplitude in the k_z direction which can be measured by the number of isolated closed-orbit islands which are crossed.

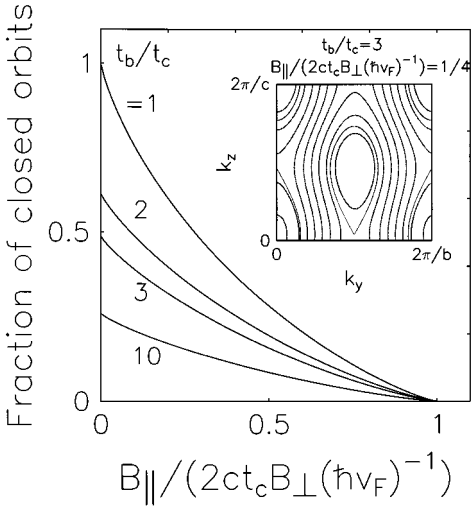

FIG. 4. The fraction of closed orbits as a function of the direction of the applied magnetic field for different values of t_b/t_c. We have chosen $\mathbf{B}_\parallel=B_\parallel\hat{\mathbf{k}}$. All the orbits become open when $B_\parallel/B_\perp \geqslant 2ct_c/\hbar v_F$. Inset: the orbits for $t_b/t_c=3$ and $B_\parallel\hbar v_F/(2ct_cB_\perp)=0.25$. The regions of closed orbits are shaded.

Considering Fig. 5(a), we can therefore say that orbits A and C each have an amplitude of 1 since they navigate around isolated islands of closed orbits in *adjacent* Brillouin zones in the k_z direction; orbit B has an amplitude of 2 since it travels across a further Brillouin zone in the k_z direction. We denote this amplitude by ζ_z and note that it is necessarily an integer.

In general, orbits of amplitude ζ_z and ζ_z+1 coexist. We find that ζ_z decreases as the in-plane magnetic field component increases. We plot the maximum of the two amplitudes $\zeta_z^{\max}$ $(=\zeta_z^{\min}+1)$ for various values of t_b/t_c and $B_\parallel$ in Fig. 5(b). This figure shows that $\zeta_z^{\max}$ decreases at particular transition points which depend on the ratio t_b/t_c. In the limit that the applied field is entirely in plane along the z direction, the orbits are all straight lines along the k_y direction.

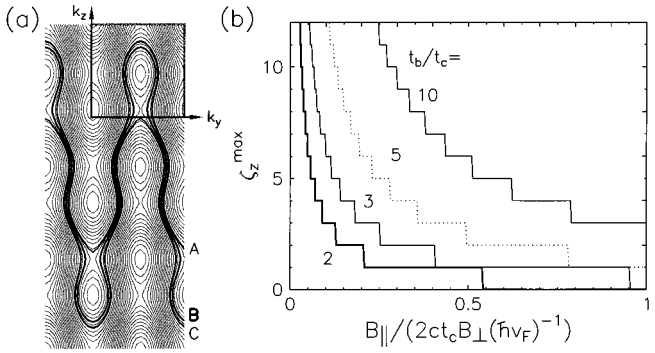

FIG. 5. (a) If the field acquires a nonzero component along the z direction, the orbits are extended along the k_y direction and exhibit a large degree of movement in the k_z direction. Each open orbit has an amplitude in the k_z direction which can be measured by the number of isolated closed-orbit islands which are crossed. Orbits A and C each have an amplitude of 1; orbit B has an amplitude of 2 (see text). (b) The maximum of amplitudes of open orbits for various values of t_b/t_c and $B_\parallel$.

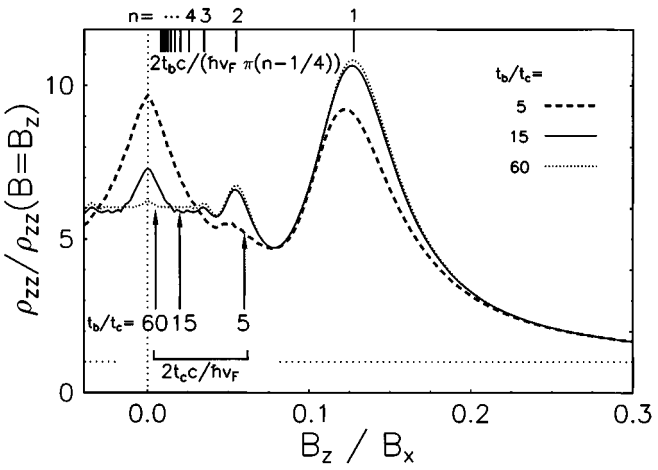

FIG. 6. Simulated resistivity for the weakly modulated FS with parameters $ev_F\tau bB/\hbar=20$ and $2t_bc/\hbar v_F=0.3$ for three values of t_b/t_c as shown in the legend. In each case, closed orbits exist only when $B_z/B_x<2t_c/\hbar v_F$ as indicated by the arrows. Resistance peaks occur when $B_z/B_x=2t_bc/\hbar v_F\pi(n-1/4)$ when $B_z/B_x\gg 2t_cc/\hbar v_F$ and these points are indicated by the vertical lines at the top of the figure. The horizontal dotted line is $\rho_{zz}=\rho_{zz}(B=B_z)$.

B. Conductivity: Danner-Wang-Chaikin oscillations

The transitions between different types of orbits which we have considered in the previous section are related to changes in the conductivity. These transitions are manifested in two particular ways.

First, we expect a larger resistance when there are closed orbits present since these are more efficient in averaging the velocity. Consequently, the resistance should change when the condition in Eq. (12) is satisfied and all orbits become open.

Second, we expect an enhancement of the velocity averaging (peaks in the resistance) associated with the transitions between the different open orbits considered in the previous section. Those transitions were based purely upon the geometrical structure of the orbits; however we now wish to find the orbits which maximise the velocity averaging. Crudely, this will occur whenever the amplitude of the open orbit in the k_z direction equals an integer times $2\pi/c$. This condition can be written

$$\Phi(k_y,k_z)=\Phi(k_y+\pi/b,k_z+2n\pi/c) \tag{13}$$

because electron trajectories are on curves of constant Φ, and this reduces to $B_z/B_x=2t_bc/\hbar v_F\pi n$ where n is an integer. A more exact treatment[23] shows that

$$B_z/B_x=2t_bc/\hbar v_F\pi(n-1/4) \tag{14}$$

when $B_z/B_x\gg 2t_cc/\hbar v_F$, i.e., when the condition for the destruction of closed orbits is substantially exceeded.

These features are illustrated in Fig. 6 which shows simulated resistivity for this FS (with parameters $ev_F\tau bB/\hbar=20$ and $2t_bc/\hbar v_F=0.3$) for three values of t_b/t_c as indicated. The existence of closed orbits is possible when $B_z/B_x<2t_c/\hbar v_F$ and is accompanied by an increase in resistance in this region which is related to the fraction of closed orbits possible (compare with the behavior in Fig. 4).

Resistance peaks are indeed observed when Eq. (14) is satisfied for integer n. However, the positions of the peaks for $t_b/t_c=5$ do not agree well with this prediction because, in this case, $2t_c/\hbar v_F$ is too large and thus the condition $B_z/B_x\gg 2t_cc/\hbar v_F$ is not well satisfied. As n increases, the heights of successive resistance peaks decrease; eventually the effect is swamped by the extremely efficient averaging provided by the presence of the closed orbits.

The strength of the magnetic field $|\mathbf{B}|$ serves only to increase the intensity of all of these features, but does not alter their individual positions. This is typical of AMROs in that the observed structure in the resistivity always depends on the orientation of the field but not on its magnitude $|\mathbf{B}|$. The strength of the magnetic field affects only the resolution of the structure.

AMROs which are very similar to those shown in Fig. 6 have been experimentally observed in $(TMTSF)_2ClO_4$ by Danner, Wang, and Chaikin by rotating the magnetic field close to the a axis.[23] Their work was the first to show that AMROs could occur by this mechanism in such a simple FS.

If the magnetic field lies in the plane of the sheets [$\mathbf{B}=(0,B\sin\theta,B\cos\theta)$], the result of the argument outlined in the next section [Eq. (29)] can be used to show that

$$\frac{\rho_{zz}(B)-\rho_{zz}(0)}{\rho_{zz}(0)}=\left(\frac{B}{B_0}\right)^2, \tag{15}$$

where $B_0=\hbar/(e\tau v_Fc\sin\theta)$. Therefore, as the magnetic field is rotated in the plane of the sheets, this model predicts no fine structure and the resistance only changes smoothly. If the FS defined in Eq. (10) is believed to be a reasonable representation of the FS in most TMTSF salts, then one would therefore conclude that a semiclassical model could not account for the sharp features and dramatic AMRO behavior which have been observed in these materials. [9,11]

However, there is some evidence that the simple picture of TMTSF salts described by Eq. (10) may be an oversimplification,[29,30] so the applicability of this model to

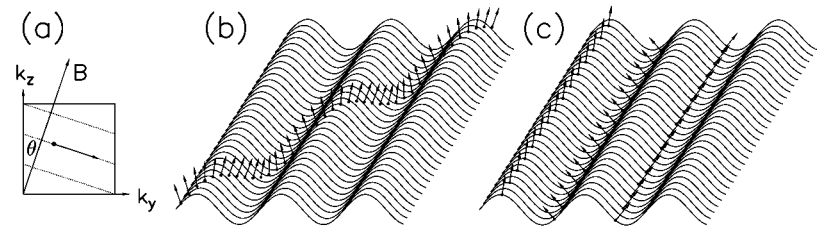

FIG. 7. (a) If magnetic field lies in the plane of the q1D sheets all orbits become straight lines when projected on to the k_y-k_z plane. For a given Fourier component of the corrugation, the velocity is more effectively averaged when electrons (b) are not traveling along the axis of the corrugation than (c) when they are.

the resistivity observed in these materials is very much an open question. We will return to this point in Sec. V.

IV. GENERAL Q1D FS

A. Introduction

When the magnetic field lies in the plane of the q1D sheets [$B_\perp = 0$ so that the magnetic field $\mathbf{B}$ is given by $\mathbf{B} = (0, B\sin\theta, B\cos\theta)$], all orbits become straight lines when projected on to the k_y–k_z plane, all lying in a direction perpendicular to the magnetic field [see Fig. 7(a)]. This case is particularly simple to analyze and analytic results can be obtained for the conductivity (see below) for any general q1D FS. The AMROs in this case arises from the fact that for any Fourier component of corrugation, the velocity is more effectively averaged when electrons are not traveling along the axis of the corrugation [Fig. 7(b)] than when they are [Fig. 7(c)]; thus sharp resistance minima are obtained when the orbits run along a Fourier component of the corrugation.

The $B_\perp = 0$ case is simple because the electron orbits are determined only by the field direction and not by the precise shape of the FS (parametrized by the t_{mn}). Thus the shape of the FS only enters the calculation at the final stage, in calculating the conductivity *given* the electron orbits. When $B_\perp \neq 0$, the t_{mn} control both the orbits *and* the resultant conductivity so that the situation is much more complicated.

The $B_\perp = 0$ calculation was first performed in Ref. 18, showing that there should be resistivity dips when $\tan\theta = (m/n)\times(b/c)$ where m and n are nonzero integers. This treatment therefore made three predictions: first, that resistivity dips in $\tan\theta$ should be observed at fractional values of b/c, as well as at integer values (when $n = 1$); second, there should be a missing dip at $m = 0$; third, the oscillations should be symmetric in $\tan\theta$. Experimentally it is found that for $(ET)_2KHg(SCN)_4$ the dips occur at

$$\tan\theta = \alpha m + \beta, \tag{16}$$

where α and β are constants, and $m = \ldots, -2, -1, 0, 1, 2, \ldots$. Therefore, fractional effects are not observed, there is no missing dip at $m = 0$ and the symmetry in $\tan\theta$ is broken by an offset.[21,22]

These differences with prediction can be understood if the Fourier components of the corrugation are defined on an oblique lattice, rather than a rectangular one. The q1D FS in Eq. (9) should therefore be further generalized as

$$E(\mathbf{k}) = \hbar v_F(|k_x| - k_F) - \sum_{m,n} [t_{mn}^{\text{even}}\cos(\mathbf{R}_{mn}\cdot\mathbf{k}_\parallel) + t_{mn}^{\text{odd}}\sin(\mathbf{R}_{mn}\cdot\mathbf{k}_\parallel)], \tag{17}$$

where $\mathbf{R}_{mn} = (0, mb + nd, nc)$ are lattice vectors on this oblique lattice (see Fig. 8). We set $t_{00}^{\text{even}} = t_{00}^{\text{odd}} = 0$ since these terms only produce a shift in the Fermi energy.

B. Calculation of ρ for the case of $B_\perp = 0$

For the FS defined in Eq. (17), the velocity $\mathbf{v}$ of each electron as a function of momentum $\mathbf{k}$ can then be calculated using $\mathbf{v}(\mathbf{k}) = \hbar^{-1}[dE(\mathbf{k})/d\mathbf{k}]$ and will be time dependent since the electron's momentum $\mathbf{k}$ varies with time according

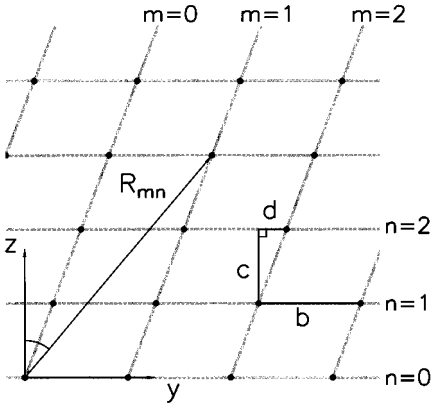

FIG. 8. Each Fourier component of the corrugation can be associated with a vector $\mathbf{R}_{mn}$ defined on an oblique grid as shown. This illustrates the definition of b, c, and d.

to the equation of motion $\hbar\dot{\mathbf{k}} = -e\mathbf{v}\times\mathbf{B}$. Thus, the in-plane components of the $\mathbf{k}$ are given by

$$\dot{k}_y = eB\hbar^{-1}v_F\,\text{sgn}(k_x)\cos\theta, \tag{18}$$

$$\dot{k}_z = -eB\sin\phi\hbar^{-1}v_F\,\text{sgn}(k_x)\sin\theta. \tag{19}$$

Hence,

$$k_y(t) = k_y(0) + eB\hbar^{-1}v_F t\,\text{sgn}(k_x)\cos\theta, \tag{20}$$

$$k_z(t) = k_z(0) - eB\hbar^{-1}v_F t\,\text{sgn}(k_x)\sin\theta, \tag{21}$$

and the electrons move in straight lines (when projected on to the k_y–k_z plane) along contours of constant $\Phi = v_F\mathbf{B}_\parallel\cdot\mathbf{k}_\parallel$. The electron velocity $\mathbf{v}(t)$ is given by

$$v_x = v_F\,\text{sgn}(k_x), \tag{22}$$

$$v_y = \hbar^{-1}\sum_{m,n}(mb + nd)[t_{mn}^{\text{even}}\sin\alpha_{mn}(t) - t_{mn}^{\text{odd}}\cos\alpha_{mn}(t)], \tag{23}$$

$$v_z = \hbar^{-1}\sum_{m,n} nc[t_{mn}^{\text{even}}\sin\alpha_{mn}(t) - t_{mn}^{\text{odd}}\cos\alpha_{mn}(t)], \tag{24}$$

where

$$\alpha_{mn}(t) = \mathbf{R}_{mn}\cdot\mathbf{k}_\parallel(0) + G_{mn}v_F t\,\text{sgn}(k_x) \tag{25}$$

and

$$G_{mn} = \frac{eB}{\hbar}[(mb + nd)\cos\theta - nc\sin\theta]. \tag{26}$$

Substituting these equations into the Boltzmann transport equation [Eq. (8)] we find that

$$\sigma_{xx} = e^2 g(E_F)v_F^2\tau \tag{27}$$

and $\sigma_{xy} = \sigma_{yx} = \sigma_{xz} = \sigma_{zx} = 0$ but

$$\begin{pmatrix} \sigma_{yy} & \sigma_{yz} \\ \sigma_{zy} & \sigma_{zz} \end{pmatrix} = \frac{e^2}{4\pi^3\hbar^2}\sum_{m,n}\sum_{m',n'}\begin{pmatrix} (m'b+n'd)(mb+nd) & (m'b+n'd)nc \\ (mb+nd)n'c & n'nc^2 \end{pmatrix} \times \int_{\mathrm{FS}} d^3\mathbf{k}(0)\left[-\frac{\partial f_0(\mathbf{k})}{\partial E(\mathbf{k})}\right][t_{mn}^{\mathrm{even}}\sin\alpha_{mn}(0) - t_{mn}^{\mathrm{odd}}\cos\alpha_{mn}(0)] \times \int_{-\infty}^{0}[t_{m'n'}^{\mathrm{even}}\sin\alpha_{m'n'}(t) - t_{m'n'}^{\mathrm{odd}}\cos\alpha_{m'n'}(t)]e^{t/\tau}dt. \tag{28}$$

After some algebra, we arrive at

$$\begin{pmatrix} \sigma_{yy} & \sigma_{yz} \\ \sigma_{zy} & \sigma_{zz} \end{pmatrix} = \frac{g(E_F)e^2\tau}{\hbar^2}\sum_{m,n}\begin{pmatrix} (mb+nd)^2 & (mb+nd)nc \\ (mb+nd)nc & (nc)^2 \end{pmatrix}\frac{t_{mn}^2}{1+(G_{mn}\tau v_F)^2}, \tag{29}$$

where $t_{mn}^2=(t_{mn}^{\mathrm{even}})^2+(t_{mn}^{\mathrm{odd}})^2$. The θ dependence is contained in G_{mn} and maxima in the conductivity are observed whenever $G_{mn}=0$, i.e.,

$$\tan\theta = \frac{m}{n}\times\frac{b}{c}+\frac{d}{c} \tag{30}$$

in agreement with the empirical result in Eq. (16) if the only significant t_{mn} occur when $n=-1,0,1$. If this last condition is not fulfilled, we would expect to see significant fractional AMRO peaks (i.e., at $m/n=1/2,1/3,2/3,3/2,\ldots$, etc.). We will discuss the significance of this condition in the following section.

The orbits corresponding to these ''resonant'' directions are periodic on the reduced Brillouin zone (i.e., the torus T^2) with period n (if m and n are relatively prime and $n\neq 0$). Orbits at a ''general'' direction ergodically fill the whole Brillouin zone. However this fact has little bearing on the resistance in this model since the contribution of such an orbit is governed by t_{mn} and will produce no resonance if $t_{mn}=0$. Thus the *geometry* of the Fermi sheet, parametrized by the Fourier components t_{mn} of the corrugation, entirely controls the AMROs in this case.

The terms $t_{mn}^2/[1+(G_{mn}\tau v_F)^2]$ in Eq. (29) are most important in governing the appearance of the AMRO minima. Increasing $B=|\mathbf{B}|$ or τ (i.e., increasing $G_{mn}v_F\tau\propto B\tau$) makes each resonance sharper (as is observed experimentally[22]); the relative height of each peak is strongly influenced by t_{mn}. As noted above, the observed features depend only on the orientation of the field and not on its magnitude $|\mathbf{B}|$, which affects only the resolution of those features.

The total conductivity is a sum (appropriately weighted) of terms associated with each Fourier component and is therefore dominated by any large term. Therefore, as discussed above, each AMRO minimum can be associated with a particular Fourier component of FS corrugation, the velocity being more effectively averaged when electrons are not traveling along the axis of this Fourier component of corrugation than when they are [Figs. 7(b) and 7(c)]. It is important to realize that a large number of Fourier components may contribute to the same AMRO peak since the terms with $m=rM$ and $n=rN$ resonate when $\tan\theta=(M/N)\times(b/c)+d/c$ for all values of the integer r. For example, this means that we cannot determine the $n=0$ Fourier components t_{m0}, but only the sum $\Sigma_{m=-\infty}^{\infty}t_{m0}^2$.

Considerable qualitative agreement with the form of the experimental data in $(\mathrm{ET})_2\mathrm{KHg(SCN)}_4$ (see, e.g., Ref. 22) can be obtained using Eq. (29), as shown in Fig. 9. As is discussed below, the component shown in Fig. 9 is the relevant experimental quantity. Substantial changes in the shape of the AMRO dips and AMRO background, together with the character of the maxima, can be achieved by adjusting the parameters t_{mn}.

This model can also be used to make predictions about the MR observed as a function of field for various orientations of the applied field (see Fig. 10). For small applied fields, ρ_{zz} is linear in B, but at higher fields it either rises as B^2 at an AMRO maximum or rises very much more slowly at an AMRO minimum (although at very high fields this will also rise as B^2). This is because the condition $G_{mn}v_F\tau\gg 1$ is reached very much more quickly at an AMRO maximum (where no G_{mn} is small) than at an AMRO minimum in which the conductivity is strongly dominated by a term for

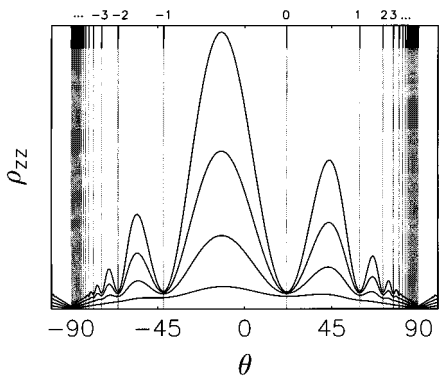

FIG. 9. Simulated AMROs using parameters chosen to mimic those fitted from experimental data in $(\mathrm{ET})_2\mathrm{KHg(SCN)}_4$ for different values of the magnetic field. We have used $b{:}c{:}d=1.3{:}1{:}0.4$, the magnetic field is $ev_FB\tau/\hbar=2.5,5,7.5,10$. The only nonzero Fourier components are $t_{01}=1$ and $t_{m1}=1/(1+m^2)$. The form of the AMROs are relatively insensitive to t_{10} in this case.

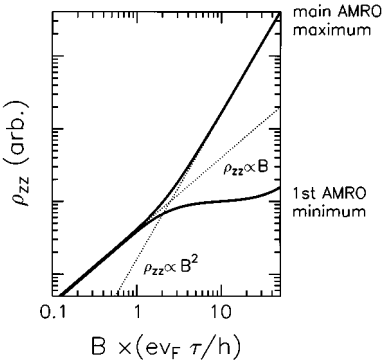

FIG. 10. Simulated MR using the same parameters as in Fig. 9 and considering the central main AMRO maximum (for which $\theta \sim -10°$, see Fig. 9) and the $m=1$ AMRO minimum (for which $\theta \sim 20°$, again see Fig. 9). Also shown as dotted lines are the functional forms $\rho_{zz} \propto B$ and $\rho_{zz} \propto B^2$.

which $G_{mn}=0$. This behavior is entirely consistent with the ''sublinear'' and ''superlinear'' MR observed at AMRO minima and maxima well below the kink transition in $(ET)_2TlHg(SCN)_4$,[31] which is expected to have a very similar FS to $(ET)_2KHg(SCN)_4$.

C. Magnetic field out of the q1D planes

If the magnetic field acquires an out-of-plane component, the calculation presented above cannot be so simply repeated. The electron orbits are no longer straight lines, but follow contours of constant $\Phi = v_F \mathbf{B}_\parallel \cdot \mathbf{k}_\parallel + B_\perp f$. However, we can neglect the last term in this expression if $B_\parallel / B_\perp \gg (b/\hbar v_F) \Sigma_{m,n} t_{mn}$ so that the magnetic field has a significant in-plane component in comparison with the corrugation. For a very weak corrugation, this will hold well until the field is close to perpendicular to the Fermi sheet. Therefore, in this case it is sufficient to use Eq. (29) with the value of the magnetic field replaced by its in-plane component.

In an AMRO experiment, resistance is recorded as a function of angle θ at various azimuthal angles ϕ describing the plane of rotation; $\phi = 0°$ represents rotation about k_x and increasing values of ϕ represent angular displacement of the rotation axis in the k_x–k_y plane towards the k_y axis; rotation about the k_y axis then corresponds to $\phi = 90°$. Experiments are usually performed by first setting ϕ at a particular fixed magnetic field and then rotating the sample (varying θ) in that magnetic field. Using the approximation described above, we can then compute the AMROs for the same parameters used for Fig. 9 yielding the simulation in Fig. 11. (This approximation is valid for $|\phi|$ sufficiently below 90°.) The simulation bears a strong resemblance to experimental data in $(ET)_2KHg(SCN)_4$.[22] It is also possible to numerically calculate these curves using the equations of motion directly (thus avoiding the necessity of invoking the approximation which fails as $|\phi|$ approaches 90°) but this is computationally much more demanding.

V. CONSEQUENCES FOR EXPERIMENTAL OBSERVATIONS

A. TMTSF salts

In the last decade or so, there has been an intensive search to find an adequate explantion for AMROs in TMTSF salts

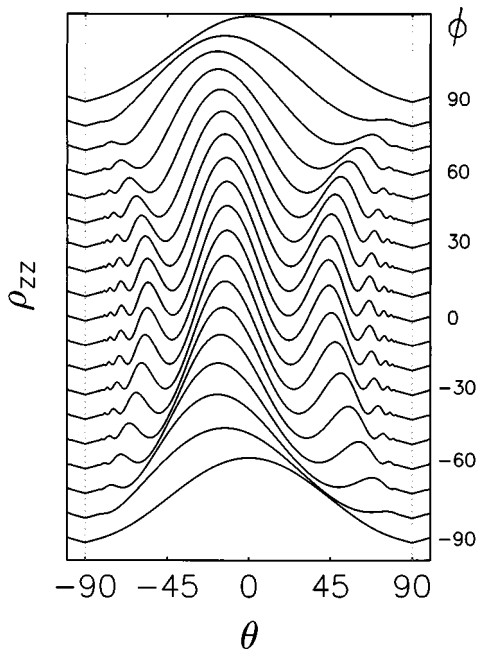

FIG. 11. Azimuthal dependence of the AMROs using the same parameters as in Fig. 9 and setting $ev_F B\tau/\hbar = 10$.

and, by extension, for any q1D metal. It was first argued that the periodic motion of the electrons at magic angles reduces the effective dimensionality of the electron-electron interactions.[12,13] This ''one-dimensionalization'' provides a strong increase in the electron-electron scattering, producing resistance peaks at the magic angles.[13,14] In experiments however, resistance *dips* are observed, rather than peaks. It has therefore been necessary to refine this model, considering an altered FS, to provide agreement with observation.[15,16] Another recent explanation of the effect is based upon the proposal that the magnetic field renormalizes the coherent part of the c-axis hopping to zero; [17] hopping parallel to the magnetic field is unaffected, so that the dips are predicted when the field points along a real space lattice vector.

There have been three approaches to explain the effect in a purely semiclassical way. In the first, Osada *et al.*[18] have considered a band structure consisting of weakly corrugated q1D sheets across which electrons travel in open orbits in which the higher order effective interchain transfer integrals t_{mn} are assumed to be significant. In the same way as shown above, they find that at particular directions of the applied magnetic field there are large resonances in the conductivity when the condition for the existence of periodic orbits of sufficiently small period is satisfied. A second approach[19] considers only the first-order transfer integrals but assumes that intersheet scattering is very high at paricular ''hot spots'' on the FS; the resistance is then determined by the rate at which electrons find these spots; at a magic angle, the periodic electron motion in the reduced zone scheme allows some fraction of the electrons to miss the hot spot; at unmagic angles, the electron trajectories are incommensurate and ergodically sweep out the whole FS, all electrons scattering strongly at the hot spots. A third model[20] considers only nearest neighbor transfer integrals but uses a nonlinearized band model, so that the corrugations are included implicitly. All three approaches predict resistance dips.

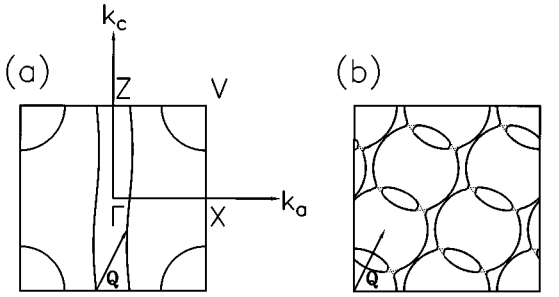

FIG. 12. Candidate Fermi surfaces for α-$ET_2KHg(SCN)_4$: (a) Calculated Fermi surface (after Ref. 33) consisting of a 2D closed hole pocket and a pair of 1D planar FS sheets. This is believed to be probably valid above T_N or in fields greater than $\sim$ 22 T. (b) Below T_N, the Fermi surface is thought to be nested by a SDW as shown (nesting vector **Q**) resulting in the destruction of the 1D planar FS sheets and the formation of new inclined open sheets and small closed pockets from the 2D closed pocket in the original FS (after Ref. 34).

As shown in Sec. III, if one does not assume the existence of higher order transfer integrals it is not possible to explain the ''in-plane'' AMROs in TMTSF salts using our approach or that of Osada *et al.*, although this can be done using the method of Ref. 20. However, the current picture of the band structure of TMTSF salts described by Eq. (10) is called into question by a number of experimental observations, chiefly the rapid oscillation phenomenon[29,30] and apparent cyclotron resonance[32] both of which imply the existence of closed FS pockets. That a semiclassical description may be relevant in these materials is supported by the observation and semiclassical explanation of the ''out-of-plane'' AMROs discovered by Danner, Wang, and Chaikin. [23]

B. $(ET)_2KHg(SCN)_4$

The case of $(ET)_2KHg(SCN)_4$ is rather different from that of $(TMTSF)_2X$. The predicted FS consists of a 2D closed hole pocket and a pair of 1D planar sheets [24,33] [Fig. 12(a)]. However, it appears that at low temperatures, below the Néel temperature T_N, a spin density wave (SDW) nests the FS so that only some small pockets and a q1D section of the FS remains; this q1D section is thought to be inclined at $\sim 21°$ to the crystallographic b^*c plane [Fig. 12(b)]. The nested FS shown in Fig. 12(b) may not be correct in every detail but probably gives a good indication of the sort of ground state that occurs. This reconstructed ground state can be destroyed by temperature (above T_N) or magnetic field (above about $B_{\rm kink} \sim 22$ T, at the so-called ''kink'' transition) so that the FS reverts back to the form shown in Fig. 12(a).[35] This picture is supported by AMRO experiments: the observed AMROs are found to be q1D in the nested region ($T<T_N$ and $B<B_{\rm kink}$) and q2D outside it ($T>T_N$ or $B>B_{\rm kink}$).[21,22,25]

This salt consists of a sandwich structure of alternate layers (along ac planes) of ET molecules and $KHg(SCN)_4^-$ anions. The ET molecules are linked to each other in these planes by overlap of their molecular π orbitals and they stack alongside one another. They are separated in the b^* direction by sheets of the anion $KHg(SCN)_4^-$, to form a 2D conductive network. The resistance is therefore much greater with the current across the planes (parallel to the b^* direction) than with it in the ac plane. In a transport experiment on this material, resistance is measured with voltage contacts placed on both ac (conducting plane) platelet faces. [22] Since the b^* axis lies along the q1D FS produced by the nesting, it is convenient to take this as the z axis and thus ρ_{zz} is the relevant experimental quantity that is of interest.

Figures 9 and 10 show that the presence of a strongly warped q1D FS, produced by nesting, results in a large positive MR away from the AMRO minima. The large temperature dependent MR that are observed in ET salts with SDW groundstates [for example, compare $(ET)_2AuBr_2$ (Ref. 36) and $(ET)_2KHg(SCN)_4$ (Ref. 22) with $(ET)_2Cu(NCS)_2$ (Ref. 37] may be partly due to the highly corrugated FS which results [and therefore reflects the temperature dependence of the scattering time τ strongly influencing the MR through the terms $G_{mn}\tau v_F$ in Eq. (29)], but spin-disorder scattering is also likely to be important.

Returning to the high field behavior, the AMROs clearly sense a FS reconstruction in $(ET)_2KHg(SCN)_4$ as the kink field is exceeded. Two serious problems with this interpretation can reasonably be posed.

First, above the kink field, the FS probably contains q1D sections as well as q2D sections [Fig. 12(a)], while below the kink field, q2D sections must occur for SdHOs to be observed,[22] in addition to the q1D sections which we believe dominate the AMROs, and are indeed present in the nested FS in Fig. 12(b). If both types of FS occur above and below the kink, why is a transition in the AMROs observed?

A second problem concerns the parameters t_{mn}; these are often related to the transfer integrals associated with the lattice vector $\mathbf{R}_{mn}$.[18] Simulations of AMROs in $(ET)_2KHg(SCN)_4$ require these to decay relatively slowly with increasing m and n in order to model the data,[26] whereas one might expect anything other than the nearest neighbor and next-nearest neighbor overlaps to be negligibly small.

The resolution of these problems is extremely instructive. The absence of ''higher order overlaps'' (i.e., significant t_{mn} for large m and n) is precisely why no AMROs due to q1D sections of the Fermi surface are generally observed in many q1D metals, and in particular, why none is observed above the kink transition in $(ET)_2KHg(SCN)_4$. The salt α-$ET_2NH_4Hg(SCN)_4$ is isostructural with $(ET)_2KHg(SCN)_4$ and is believed to have a FS identical with that in Fig. 12(a).[24] This salt undergoes no low field SDW transition [and thus no consequent FS reconstruction) and hence shows only q2D AMROs. Therefore, although q1D sheets are present in α-$ET_2NH_4Hg(SCN)_4$ (and also in α-$ET_2KHg(SCN)_4$ above the kink transition], q1D AMROs are not seen from them because they are insufficiently corrugated. The AMRO is then dominated by the q2D sections.

However, below the kink in α-$ET_2KHg(SCN)_4$, the nesting of the FS removes the weakly corrugated q1D sections of FS and ''cuts up and glues together'' pieces of q2D FS. The reconstructed FS then consists of a very highly and irregularly corrugated Fermi sheet since it consists of a periodic assembly of cylindrical sections [see Fig. 12(b)]; the corrugation thus has a very high harmonic content. In consequence, the t_{mn} should not be interpreted here as transfer integrals so much as Fourier components of the corrugation.

This fact has been pointed out in Ref. 18. Although some q2D pockets are also formed in the reconstructed FS, these do not contribute to the AMROs. This is perhaps because they themselves are irregularly corrugated; the q2D AMRO effect relies on cylindrical sections of FS with relatively *weak and regular* corrugation. Because the q1D Fermi sheet is automatically much more irregularly corrugated in one direction than in the other, this provides a natural explanation for why the contributing Fourier components have all values m but only $n=-1,0,1$, so that only integer, rather than fractional AMROs, are observed. The obliqueness of the lattice on which the corrugations are defined (see Fig. 8) reflects the structure of the q1D Fermi sheet which is at an angle ($\sim 21°$) to the (triclinic) crystallographic axes in $(ET)_2KHg(SCN)_4$ (specifically, the b^*c plane). It is important to emphasize that the information obtained from AMRO experiments about the vectors $\mathbf{R}_{mn}$ concerns the geometry of the corrugations of the Fermi sheet (produced by the SDW nesting), and is not primarily related to the crystallographic geometry.

VI. SUMMARY

We have described a semiclassical approach to calculate the AMROs for a completely general class of q1D Fermi surfaces. Higher order Fourier components in the corrugation of the Fermi sheet are essential to explain the observed AMROs and the size of the MR in $(ET)_2KHg(SCN)_4$. Our approach stresses the geometrical structure of the corrugated FS as parametrized by Fourier components t_{mn}; these components should often *not* be interpreted as overlap integrals.

AMROs observed in $(TMTSF)_2ClO_4$ when the magnetic field is rotated close to the a axis are of a different character and reflect the evolution of particular types of open and closed orbits. The q1D AMROs are absent in most organic metals with q1D Fermi surfaces because they are not sufficiently corrugated. Weakly corrugated q1D sheets will not contribute significantly to the angle-dependent MR and will not give rise to any sharp features. Because q1D AMROs will therefore only be seen when the q1D sheets are highly corrugated, lack of q1D AMROs cannot be taken as proof of nesting of 1D parts of FS. The form of the corrugation of the q1D sheets deduced from AMRO data in $(ET)_2KHg(SCN)_4$ is consistent with the model of the nested FS which has been proposed to explain the low field, low temperature ground state.

The results of AMRO experiments can therefore be extremely useful in trying to understand the electronic structure of organic metals. Not only can they probe the warping of 2D sections of FS, but they can measure the Fourier components of the corrugation of highly irregular sections of q1D FS, such as are found in density wave ground states. In contrast to SdHo, the effect is due to all electrons on the Fermi surface, not just those performing closed extremal orbits, and can therefore give unique information.

ACKNOWLEDGMENTS

We are grateful to the EPSRC and the Royal Society for financial support and to K. M. Blundell for helpful comments on the manuscript.

[1] A. B. Pippard, *Magnetoresistance in Metals* (Cambridge University Press, Cambridge, 1989).
[2] D. Shoenberg, *Magnetic Oscillations in Metals* (Cambridge University Press, Cambridge, 1984).
[3] For a recent review, see *The Proceedings of the International Conference of Synthetic Metals*, Seoul, Korea, 1994 [Synth. Met. **69-71** (1995)].
[4] K. Yamaji, J. Phys. Soc. Jpn. **58**, 1520 (1989).
[5] M. V. Kartsovnik, V. N. Laukhin, S. I. Pesotskii, I. F. Schegolev, and V. M. Yakovenko, J. Phys. I **2**, 89 (1993).
[6] D. Jerome and H. J. Schulz, Adv. Phys. **31**, 299 (1982).
[7] T. Ishiguro and K. Yamaji, *Organic Superconductors* (Springer-Verlag, Berlin, 1990).
[8] W. Kang, S. T. Hannahs, and P. M. Chaikin, Phys. Rev. Lett. **70**, 3091 (1993).
[9] G. S. Boebinger, G. Montambaux, M. L. Kaplan, R. C. Haddon, S. V. Chichester, and L. Y. Chiang, Phys. Rev. Lett. **64**, 591 (1990).
[10] T. Osada, A. Kawasumi, S. Kagoshima, N. Miura, and G. Saito, Phys. Rev. Lett. **66**, 1525 (1991).
[11] W. Kang, S. T. Hannahs, and P. M. Chaikin, Phys. Rev. Lett. **69**, 2827 (1992).
[12] L. P. Gor'kov and A. G. Lebed, J. Phys. (Paris) Lett. **45**, 833 (1984); P. M. Chaikin, Phys. Rev. B **31**, 4770 (1985).
[13] A. G. Lebed, JETP Lett. **43**, 174 (1986).
[14] A. G. Lebed and P. Bak, Phys. Rev. Lett. **63**, 1315 (1989).
[15] A. G. Lebed, J. Phys. I (France) **4**, 351 (1994).
[16] A. G. Lebed, Synth. Met. **70**, 993 (1995).
[17] S. P. Strong, D. G. Clarke, and P. W. Anderson, Phys. Rev. Lett. **73**, 1007 (1994).
[18] T. Osada, S. Kagoshima, and N. Miura, Phys. Rev. B **46**, 1812 (1992).
[19] P. M. Chaikin, Phys. Rev. Lett. **69**, 2831 (1992).
[20] K. Maki, Phys. Rev. B **45**, 5111 (1992).
[21] T. Sasaki and N. Toyota, Phys. Rev. B **49**, 10 120 (1994).
[22] J. Caulfield, S. J. Blundell, M. S. L. du Croo de Jongh, P. T. J. Hendriks, J. Singleton, M. Doporto, F. L. Pratt, A. House, J. A. A. J. Perenboom, W. Hayes, M. Kurmoo, and P. Day, Phys. Rev. B **51**, 8325 (1995).
[23] G. M. Danner, W. Kang, and P. M. Chaikin, Phys. Rev. Lett. **72**, 3714 (1994).
[24] H. Mori, S. Tanaka, M. Oshima, G. Saito, T. Mori, Y. Maruyama, and H. Inkuchi, Bull. Chem. Soc. Jpn. **63**, 2183 (1990).
[25] J. Caulfield, J. Singleton, P. T. J. Hendriks, J. A. A. J. Perenboom, F. L. Pratt, M. Doporto, W. Hayes, M. Kurmoo and P. Day, J. Phys. Condens. Matter **6**, L155 (1994).
[26] Y. Iye, R. Yagi, N. Hanasaki, S. Kagoshima, H. Mori, H. Fujimoto, and G. Saito, J. Phys. Soc. Jpn. **63**, 674 (1994).
[27] D. K. Arrowsmith and C. M. Place, *An Introduction to Dynamical Systems* (Cambridge University Press, Cambridge, 1990).
[28] M. Nakahara, *Geometry, Topology and Physics* (Adam Hilger, London, 1990).

[29] J. P. Ulmet *et al.*, Solid State Commun. **58**, 253 (1986); X. Yan *et al.*, Phys. Rev. B **36**, 1799 (1987); A. Audouard *et al.*, *ibid.* **50**, 12726 (1994).

[30] R. H. McKenzie, J. S. Brooks, R. G. Clark, R. Newbury, R. P. Starrett, A. V. Skougarevsky, R. A. Lewis, S. Takasaki, J. Yamada, H. Anzai, Y. Tanaka, T. Kinoshita, N. Kinoshita, M. Tokumoto, and M. Kartsovnik (unpublished); also J. S. Brooks, R. G. Clark, R. H. McKenzie, R. Newbury, R. P. Starrett, A. V. Skougarevsky, M. Tokumoto, S. Takasaki, J. Yamada, and H. Anzai (unpublished).

[31] G. J. Athas, J. S. Brooks, S. Valfells, S. J. Klepper, M. Tokumoto, N. Kinoshita, M. Tokumoto, and H. Anzai, Phys. Rev. B **50**, 17713 (1994).

[32] A. S. Perel, J. S. Brooks, C. J. G. M. Langerak, T. J. B. M. Janssen, J. Singleton, J. A. A. J. Perenboom, and L. Y. Chiang, Phys. Rev. Lett. **67**, 2072 (1991).

[33] M. Oshima, H. Mori, G. Saito, and K. Oshima, Chem. Lett. **1989**, 1159 (1989).

[34] M. V. Kartsovnik, A. E. Kovalev, and N. D. Kushch, J. Phys. I (France) **3**, 1187 (1993).

[35] T. Sasaki, N. Toyota, M. Tokumoto, N. Kinoshita, and H. Anzai, Solid State Commun. **75**, 93 (1990); T. Sasaki and N. Toyota, *ibid.* **82**, 447 (1992); T. Sasaki, H. Sato, and N. Toyota, Synth. Met. **42**, 2211 (1991); S. J. Klepper, J. S. Brooks, G. J. Athas, X. Chen, M. Tokumoto, N. Kinoshita, and Y. Tanaka, Surf. Sci **305**, 181 (1994); T. Osada, R. Yagi, A. Kawasumi, S. Kagoshima, N. Miura, M. Oshima, T. Nakamura, and G. Saito, Synth. Met. **42**, 2171 (1991); T. Osada, R. Yagi, S. Kagoshima, N. Miura, M. Oshima, and G. Saito, Phys. Rev. B **41**, 5428 (1990); F. L. Pratt, J. Singleton, M. Doporto, A. J. Fisher, T. J. B. M. Janssen, J. A. A. J. Perenboom, M. Kurmoo, and P. Day, *ibid.* **45**, 13 904 (1992); J. S. Brooks, C. C. Agosta, S. J. Klepper, M. Tokomoto, N. Kinoshita, H. Anzai, S. Uji, H. Aoki, A. S. Perel, G. J. Athas, and D. A. Howe, Phys. Rev. Lett. **69**, 156 (1992).

[36] M. Doporto, J. Singleton, F. L. Pratt, J. Caulfield, W. Hayes, J. A. A. J. Perenboom, I. Deckers, G. Pitsi, M. Kurmoo, and P. Day, Phys. Rev. B **49**, 3934 (1994).

[37] F. L. Pratt, M. Doporto, W. Hayes, J. Singleton, T. Janssen, M. Kurmoo, and P. Day, Synth. Met. **41**, 2195 (1991); J. Caulfield, W. Lubczynski, F. L. Pratt, J. Singleton, D. Y. K. Ko, W. Hayes, M. Kurmoo, and P. Day, J. Phys.: Condens. Matter **6**, 2911 (1994).